Research Article Vol. 61, No. 33 / 20 November 2022 / Applied Optics 10049

applied optics

Efficiency enhancement of ultrathin CIGS solar cells by optimal bandgap grading. Part II: finite-difference algorithm and double-layer antireflection coatings

Faiz Ahmad,[1] Benjamin J. Civiletti,[2] Peter B. Monk,[2] and Akhlesh Lakhtakia[1,*]

[1]The Pennsylvania State University, Department of Engineering Science and Mechanics, NanoMM–Nanoengineered Metamaterials Group, University Park, Pennsylvania 16802, USA
[2]University of Delaware, Department of Mathematical Sciences, 501 Ewing Hall, Newark, Delaware 19716, USA
*Corresponding author: akhlesh@psu.edu

Received 5 September 2022; revised 13 October 2022; accepted 16 October 2022; posted 17 October 2022; published 18 November 2022

In Part I [Appl. Opt. 58, 6067 (2019)], we used a coupled optoelectronic model to optimize a thin-film $CuIn_{1-\xi}Ga_{\xi}Se_2$ (CIGS) solar cell with a graded-bandgap photon-absorbing layer and a periodically corrugated backreflector. The increase in efficiency due to the periodic corrugation was found to be tiny and that, too, only for very thin CIGS layers. Also, it was predicted that linear bandgap-grading enhances the efficiency of the CIGS solar cells. However, a significant improvement in solar cell efficiency was found using a nonlinearly (sinusoidally) graded-bandgap CIGS photon-absorbing layer. The optoelectronic model comprised two submodels: optical and electrical. The electrical submodel applied the hybridizable discontinuous Galerkin (HDG) scheme directly to equations for the drift and diffusion of charge carriers. As our HDG scheme sometimes fails due to negative carrier densities arising during the solution process, we devised a new, to the best of our knowledge, computational scheme using the finite-difference method, which also reduces the overall computational cost of optimization. An unfortunate normalization error in the electrical submodel in Part I came to light. This normalization error did not change the overall conclusions reported in Part I; however, some specifics did change. The new algorithm for the electrical submodel is reported here along with updated numerical results. We re-optimized the solar cells containing a CIGS photon-absorbing layer with either (i) a homogeneous bandgap, (ii) a linearly graded bandgap, or (iii) a nonlinearly graded bandgap. Considering the meager increase in efficiency with the periodic corrugation and additional complexity in the fabrication process, we opted for a flat backreflector. The new algorithm is significantly faster than the previous algorithm. Our new results confirm efficiency enhancement of 84% (resp. 63%) when the thickness of the CIGS layer is 600 nm (resp. 2200 nm), similarly to Part I. A hundredfold concentration of sunlight can increase the efficiency by an additional 27%. Finally, the currently used 110-nm-thick layer of MgF_2 performs almost as well as optimal single- and double-layer antireflection coatings.

https://doi.org/10.1364/AO.474920

1. INTRODUCTION

Photovoltaic solar cells (PVSCs) are eco-friendly energy sources of huge importance during the current climate emergency. Worldwide, the primary energy consumption was 154,750 terawatt-hour (TWh) in 2020, but PVSCs were used to generate only 855.7 TWh [1]. The PVSC share must grow from the current ∼0.55% to about 20% in less than three decades, as diverse industrial and transportation sectors are electrified to meet ambitious but necessary decarbonization goals [2,3]. Therefore, increasing the power-conversion efficiency, and thereby reducing the levelized cost of electricity [4] generated by PVSC modules, is essential.

Thin-film PVSCs are a promising alternative to wafer-based crystalline-silicon solar cells with significantly reduced material consumption and the promise of reduced manufacturing costs. These types of PVSCs could be employed on many kinds of exterior and interior surfaces to not only harvest direct as well as diffuse solar energy but also to recycle electrically generated light in habitable spaces. The major areas of improvements in thin-film PVSCs include but are not limited to light-trapping strategies to harvest more photons [5–8], new semiconductors with more efficient conversion of photons into charge carriers [9], bandgap grading of semiconductors [10,11], and back-surface passivation [12].

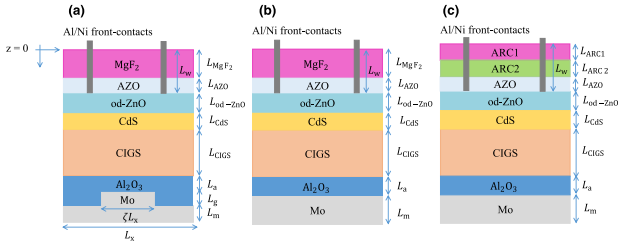

Fig. 1. (a) Schematics of CIGS thin-film solar cell with (a) a magnesium-fluoride antireflection coating and a periodically corrugated backreflector, (b) a magnesium-fluoride antireflection coating and a flat backreflector, and (c) a double-layer antireflection coating and a flat backreflector.

In the predecessor paper [13], hereafter referred to as Part I, we optimized thin-film PVSCs employing $CuIn_{1-\xi}Ga_{\xi}Se_2$ (CIGS), a quaternary I-III-VI semiconductor, as the photon-absorbing and charge-carrier-generating material. The structure of this solar cell is shown in Fig. 1(a). The bandgap energy in the p-type CIGS layer of thickness $L_{\text{CIGS}} \leq 2200$ nm was taken to be graded in the thickness direction (i.e., parallel to the z axis). The potential of guided-wave modes (i.e., surface-plasmon-polariton waves and waveguide modes [14–21]) for the enhancement of optical absorption and, therefore, the electron-hole-pair (EHP) generation rate was assessed by incorporating a periodically corrugated molybdenum (Mo) backreflector with period L_x along the x axis, duty cycle $\zeta \in (0, 1)$, and height L_g. A coupled optoelectronic model was devised to determine the power-conversion efficiency denoted by η. It was found that periodic corrugations (with $L_x \in [300, 800]$ nm and $L_g \leq 100$ nm) increased η slightly, but only for $L_{\text{CIGS}} \leq 600$ nm. Also, it was predicted that judiciously selected compositional-grading profiles (i.e., ξ as a function of z) leading to bandgap grading [22] in the CIGS layer can enhance the efficiency, with nonlinear-bandgap grading being more effective than linear-bandgap grading.

The optoelectronic model used in Part 1 [13] comprises two submodels: optical and electrical. The optical submodel is based on the rigorous coupled-wave approach (RCWA) [23,24], which simplifies to the standard transfer-matrix approach [25] for flat backreflectors. The output of the optical submodel is the EHP generation rate $G(z)$ inside the semiconductor layers of the solar cell, assuming normal illumination by unpolarized polychromatic light endowed with the AM1.5G solar spectrum. Then $G(z)$ is used in the electrical submodel as an input to the drift-diffusion system to obtain the charge-carrier fluxes and, hence, the current J_{dev} generated by the solar cell as well as the electrical power density $P = J_{\text{dev}} V_{\text{ext}}$ as functions of the bias voltage V_{ext} under steady-state conditions. In turn, the $J_{\text{dev}} - V_{\text{ext}}$ and the $P - V_{\text{ext}}$ curves yield η along with the short-circuit current density J_{sc}, open-circuit voltage V_{oc}, and fill factor FF.

As the complexity of the designs being considered by us increased, optimization became computationally expensive—because negative charge-carrier densities or overflows were encountered during the solution of the nonlinear equations arising from our implementation of the hybridizable discontinuous Galerkin (HDG) scheme [24,26]. Therefore, we devised a new solution strategy to implement a special finite-difference method (FDM) [27] utilizing quasi-Fermi potentials to provide a more robust electrical submodel and thus speed up the optimization. During this process, unfortunately, we found a normalization error in the electrical-submodel code used for Part I [13]. This normalization error does not change the overall conclusions reported in Ref. [13]; however, some specifics do change. Here, we report details of the new and more robust solution algorithm and updated numerical results. We re-optimized the CIGS solar cells containing a CIGS photon-absorbing layer with either (i) a homogeneous bandgap, (ii) a linearly graded bandgap, or (iii) a nonlinearly graded bandgap.

With $L_g = 0$, as shown in Fig. 1(b), the CIGS solar cell has a MgF_2/AZO/od–ZnO/CdS/CIGS/Al_2O_3/Mo multilayered structure. The 110-nm-thick MgF_2 layer acts as an antireflection coating. Electrons are collected in the 100-nm-thick aluminum-doped zinc oxide (AZO) layer, while the 80-nm-thick layer of oxygen-deficient zinc oxide (od-ZnO) and the 70-nm-thick layer of cadmium sulfide (CdS) function as n-type semiconductors. The photon-absorbing layer of p-type CIGS is of thickness $L_{\text{CIGS}} \leq 2200$ nm, Al_2O_3 is a 50-nm-thick passivation layer, and the Mo layer serves as both the back-contact and optical reflector.

As the effects of defects at the CdS/CIGS interface on the solar-cell performance were found in Part I [13] to be insignificant, we ignored a 10-nm-thick surface-defect layer between the CdS and CIGS layers for all results presented here. The usefulness of the Al_2O_3 passivation layer between the CIGS absorber and the Mo back-contact was established in Part I [13] to improve both J_{sc} and V_{oc}. Hence, the 50-nm-thick Al_2O_3 layer in Fig. 1(b) was considered for all results presented here except for validation against experimental results.

One method to improve the efficiency and thereby reduce the levelized cost of electricity is to use optical concentrators to increase the intensity of sunlight incident on the solar cell's surface. A significant improvement in the efficiency of thin-film graded-bandgap CIGS solar cells was reported with concentrated sunlight in Ref. [28]. The overall conclusions in that work hold true after the correction of the normalization error in the electrical-submodel code. However, as the specifics of the data reported were impacted, here we are also reporting the revised data on CIGS solar cells with concentrated sunlight.

Another way to improve the efficiency of PVSCs is by using better antireflection coatings (ARCs) and thereby enhance photon absorption by reducing reflection loss [8]. In thin-film CIGS solar cells, a single-layer antireflection coating (SLARC) of MgF_2 is used to reduce the reflection loss as shown in Fig. 1(b). However, SLARCs can be effective only in narrow spectral regimes [29,30]. So, multilayer ARCs or graded-index antireflection structures are required to reduce the reflection loss over a broad spectral regime [8]. But graded-index antireflection structures such as moth-eye and nanowire structures [31,32] bring additional cost and complexity to the manufacturing process. In contrast, multi-layer ARCs are simple to deposit using techniques such as thermal evaporation, reactive sputtering, and plasma-enhanced chemical vapor deposition.

The commonly used materials for ARCs are SiO_2, ZnS, TiO_2, ZrO_2, Si_3N_4, and Al_2O_3 [32–34]. One approach can be to maximize η by confining attention to a selection of specific materials. Another approach can be to confine attention to a

specific range of the refractive index and predict the optimal refractive index for the ARC. The commonly used approach is the former, but the latter can provide a better ARC as it considers a complete range of possible materials instead of a fixed few options; we opted for the latter approach. Hence, we optimized the refractive indices and thicknesses of SLARCs and double-layer antireflection coatings (DLARCs) for CIGS solar cells containing a CIGS photon-absorbing layer with either (i) a homogeneous bandgap, (ii) a linearly graded bandgap, or (iii) a nonlinearly graded bandgap. The structure of this solar cell is schematically depicted in Fig. 1(c). A relative enhancement of no more than 2% is predicted with an optimal DLARC compared to the efficiency with a SLARC, indicating that the simpler option of a SLARC may be economically preferable.

This paper is organized as follows. Section 2 on optoelectronic optimization is divided into five subsections. The bandgap-grading profiles chosen for the CIGS layer are presented in Section 2.A, the optical description of and the calculations for the solar cell are presented in Section 2.B, the electrical description of the solar cell and the electrical computations are described in Section 2.C, the new FDM algorithm for the solution of the drift-diffusion system is described in Section 2.D, and the optimization technique is mentioned in Section 2.E for completeness.

Numerical results are presented and discussed in Section 3, divided into eight subsections. Section 3.A compares the efficiency of the conventional 2200-nm-thick solar cell with a homogeneous CIGS layer predicted by the model with available experimental data. Section 3.B provides the optimal results for solar cells with a homogeneous CIGS layer and Section 3.C for solar cells with a linearly graded CIGS layer. Optimal results for solar cells with a nonlinearly graded-bandgap CIGS layer are discussed in Section 3.D. A detailed study of the optimal 600-nm-thick solar cell is presented in Section 3.E. Section 3.F provides the optimal results for solar cells illuminated by concentrated sunlight, and Section 3.G provides the optimal results for solar cells with double-layer antireflection coatings. The computational times needed for one run of the optoelectronic model, with the electrical submodel using either (i) the HDG scheme of Part I or (ii) the FDM scheme in the new solution strategy, are compared in Section 3.H. The paper ends with concluding remarks in Section 4.

2. OPTOELECTRONIC OPTIMIZATION

As stated earlier, we chose the solar-cell structure depicted in Fig. 1(b) with $L_{\mathrm{MgF_2}} = 110$ nm, $L_{\mathrm{AZO}} = 100$ nm, $L_{\mathrm{od\text{–}ZnO}} = 80$ nm, $L_{\mathrm{CdS}} = 70$ nm, $L_{\mathrm{CIGS}} \in [100, 2200]$ nm, $L_{\mathrm{a}} = 50$ nm, and $L_{\mathrm{m}} = 500$ nm.

A. Bandgap Energy in the CIGS Layer

The linearly nonhomogeneous bandgap energy for forward grading was modeled as

$$\mathrm{E}_g(z) = \mathrm{E}_{g,\min} + A\left(\mathrm{E}_{g,\max} - \mathrm{E}_{g,\min}\right) \frac{z - (L_w + L_{\mathrm{od\text{–}ZnO}} + L_{\mathrm{CdS}})}{L_{\mathrm{CIGS}}}, \quad z \in [L_w + L_{\mathrm{od\text{–}ZnO}} + L_{\mathrm{CdS}},\, L_d]\,. \tag{1}$$

where $\mathrm{E}_{g,\min}$ is the minimum bandgap energy, $\mathrm{E}_{g,\max}$ is the maximum bandgap energy, A is an amplitude (with $A = 0$ representing a homogeneous CIGS layer), $L_w = L_{\mathrm{MgF_2}} + L_{\mathrm{AZO}}$, and $L_d = L_w + L_{\mathrm{od\text{–}ZnO}} + L_{\mathrm{CdS}} + L_{\mathrm{CIGS}}$. The linearly nonhomogeneous bandgap energy for the backward grading was modeled as

$$\mathrm{E}_g(z) = \mathrm{E}_{g,\max} - A\left(\mathrm{E}_{g,\max} - \mathrm{E}_{g,\min}\right) \frac{z - (L_w + L_{\mathrm{od\text{–}ZnO}} + L_{\mathrm{CdS}})}{L_{\mathrm{CIGS}}}, \quad z \in [L_w + L_{\mathrm{od\text{–}ZnO}} + L_{\mathrm{CdS}},\, L_d]\,. \tag{2}$$

The parameter space for optimization of η was fixed as follows: $A \in [0, 1]$, $\mathrm{E}_{g,\min} \in [0.947, 1.626]$ eV, and $\mathrm{E}_{g,\max} \in [0.947, 1.626]$ eV with the condition $\mathrm{E}_{g,\max} \geq \mathrm{E}_{g,\min}$.

The nonlinearly varying bandgap energy was modeled with the help of sinusoidal functions as

$$\mathrm{E}_g(z) = \mathrm{E}_{g,\min} + A\left(1.626 - \mathrm{E}_{g,\min}\right) \times \left\{\frac{1}{2}\left[\sin\left(2\pi K \frac{z - (L_w + L_{\mathrm{od\text{–}ZnO}} + L_{\mathrm{CdS}})}{L_{\mathrm{CIGS}}} - 2\pi\psi\right) + 1\right]\right\}^{\alpha}, \quad z \in [L_w + L_{\mathrm{od\text{–}ZnO}} + L_{\mathrm{CdS}},\, L_d]\,, \tag{3}$$

where $\psi \in [0, 1]$ quantifies a relative phase shift, K is the number of periods in the CIGS layer, and $\alpha > 0$ is a shaping parameter. The parameter space for optimization of η was fixed as follows: $A \in [0, 1]$, $\mathrm{E}_{g,\min} \in [0.947, 1.626]$ eV, $\alpha \in [0, 8]$, $K \in [0, 8]$, and $\psi \in [0, 1]$.

B. Optical Description and Calculations

The optical description and calculations remain unchanged as discussed in Part I [13]. Spectrums of the real and imaginary parts of the relative permittivity $\varepsilon(\lambda_0)/\varepsilon_0$ of $\mathrm{MgF_2}$ [35], AZO [36], od-ZnO [37], CdS [38], CIGS [39,40], $\mathrm{Al_2O_3}$ [41], and Mo [42] used in our calculations are available in Part I [13] and Ref. [24], where $\varepsilon(\lambda_0)$ is the permittivity as a function of the free-space wavelength λ_0 and ε_0 is the permittivity of free space.

The transfer-matrix method [25] was used to calculate the electric field phasor $\mathbf{E}(z, \lambda_0) = E_x(z, \lambda_0)\hat{\mathbf{u}}_x$ everywhere inside the solar cell as a result of illumination by a monochromatic plane wave normally incident on the plane $z = 0$ from the half space $z < 0$, where $\hat{\mathbf{u}}_x$ is the unit vector parallel to the x axis. The electric field phasor of the incident plane wave was taken as

$$\mathbf{E}_{\mathrm{inc}}(z, \lambda_0) = E_0 \hat{\mathbf{u}}_x \exp\left(i 2\pi \frac{z}{\lambda_0}\right), \tag{4}$$

where $E_0 = 4\sqrt{15\pi}\ \mathrm{V\,m^{-1}}$. Standard boundary conditions were enforced on the planes $z = 0$ and $z = L_t = L_d + L_a + L_m$ to match the internal field phasors to the incident, reflected, and transmitted field phasors, as appropriate.

With the assumption that every absorbed photon excites an EHP, the EHP generation rate was calculated as

$$G(z) = \frac{\eta_0}{\hbar E_0^2} \int_{\lambda_{0,\min}}^{\lambda_{0,\max}} \mathrm{Im}\{\varepsilon(z, \lambda_0)\} |E_x(z, \lambda_0)|^2 S(\lambda_0) \mathrm{d}\lambda_0 \tag{5}$$

for $z \in [L_w, L_d]$, where η_0 is the intrinsic impedance of free space, $\hbar$ is the reduced Planck constant, $S(\lambda_0)$ is the AM1.5G solar spectrum [43], $\lambda_{0,\min} = 300$ nm, and $\lambda_{0,\max} = (1240/\mathrm{E}_{g,\min})$ eV nm.

C. Electrical Description and Calculations

The electrical description and theory remain unchanged from Part I [13]. Under steady-state conditions, the 1D drift-diffusion system comprises the following three differential equations:

$$\frac{d}{dz}J_n(z) = -q_e[G(z) - R(n, p; z)], \tag{6}$$

$$\frac{d}{dz}J_p(z) = q_e[G(z) - R(n, p; z)], \tag{7}$$

$$\frac{d}{dz}\left[\varepsilon_{dc}(z)\frac{d}{dz}\phi(z)\right] = -\frac{q_e}{\varepsilon_0}\left[N_f(z) + N_D(z) + p(z) - n(z)\right]. \tag{8}$$

These differential equations hold for $z \in (L_w, L_d)$, with $q_e = 1.602 \times 10^{-19}$ C as the elementary charge, $J_n(z)$ as the electron current density, $J_p(z)$ as the hole current density, $n(z)$ as the electron density, $p(z)$ as the hole current density, $R(n, p; z)$ as the EHP recombination rate, $N_f(z)$ as the defect density (also called trap density), $N_D(z)$ as the doping density that is positive for donors and negative for acceptors, $\phi(z)$ as the d.c. electric potential, and $\varepsilon_{\mathrm{dc}}(z)$ as the d.c. relative permittivity. The radiative EHP recombination process—depending on both charge carrier densities and the intrinsic carrier density $n_i(z)$—was incorporated in the electrical submodel [13]. The Shockley–Read–Hall EHP recombination process—depending on $n(z)$, $p(z)$, $n_i(z)$, the trap energy level E_T, and the minority carrier lifetime—was incorporated in the electrical submodel [13] as well.

The current densities are written as

$$\left.\begin{aligned} J_n(z) &= \mu_n n(z)\tfrac{d}{dz}\mathrm{E}_{F_n}(z) \\ J_p(z) &= \mu_p p(z)\tfrac{d}{dz}\mathrm{E}_{F_p}(z) \end{aligned}\right\}, \quad z \in (L_w, L_d), \tag{9}$$

where μ_n and μ_p are the electron mobility and hole mobility, respectively. The electron quasi-Fermi level

$$\mathrm{E}_{F_n}(z) = \mathrm{E}_c(z) + k_B T \ln[n(z)/N_c(z)] \tag{10a}$$

and the hole quasi-Fermi level

$$\mathrm{E}_{F_p}(z) = \mathrm{E}_v(z) - k_B T \ln[p(z)/N_v(z)] \tag{10b}$$

involve the Boltzmann constant $k_B = 1.380649 \times 10^{-23}$ J K^{-1} and the absolute temperature T, with $N_c(z)$ as the density of states in the conduction band, $N_v(z)$ as the density of states in the valence band,

$$\mathrm{E}_c(z) = \mathrm{E}_0 - [q_e\phi(z) + \chi(z)] \tag{10c}$$

as the conduction band-edge energy,

$$\mathrm{E}_v(z) = \mathrm{E}_c(z) - \mathrm{E}_g(z) \tag{10d}$$

as the valence band-edge energy, E_0 as an arbitrary reference energy level, and $\chi(z)$ as the bandgap-dependent electron affinity.

In contrast to the solution algorithm adopted for Part I, we used the quasi-Fermi levels E_{F_n} and E_{F_p} as the unknown functions to be determined by the FDM, and we computed the electron and hole densities via Eqs. (10a) and (10b). The use of the quasi-Fermi levels ensures that $n(z) \geq 0$ and $p(z) \geq 0$. See Ref. [44] for more details.

The Boltzmann approximation yields

$$J_n(z) = -q_e\mu_n(z)\left\{n(z)\frac{d}{dz}[\phi(z) + \phi_n(z)] - \frac{k_B T}{q_e}\frac{d}{dz}n(z)\right\} \tag{11a}$$

and

$$J_p(z) = -q_e\mu_p(z)\left\{p(z)\frac{d}{dz}[\phi(z) + \phi_p(z)] + \frac{k_B T}{q_e}\frac{d}{dz}p(z)\right\}, \tag{11b}$$

where

$$\phi_n(z) = \left\{\chi(z) + k_B T \ln\left[\frac{N_c(z)}{N_0}\right]\right\}/q_e \tag{12a}$$

and

$$\phi_p(z) = \left\{\chi(z) + \mathrm{E}_g(z) - k_B T \ln\left[\frac{N_v(z)}{N_0}\right]\right\}/q_e \tag{12b}$$

are the built-in potentials for electrons and holes due to variations in the material properties. The baseline number density N_0 is arbitrary because potentials are defined uniquely only up to a constant.

In order to formulate boundary conditions, ideal ohmic contacts were assumed for the planes $z = L_w$ and $z = L_d$, and the Al_2O_3 layer was ignored [24].

D. FDM Algorithm

The computational solution process of the drift-diffusion system in Part I employed the HDG scheme [45,46]. A more robust algorithm based on the FDM was devised, as stated earlier.

First the drift-diffusion system is non-dimensionalized by defining the dimensionless height

$$\bar{z} = \frac{1}{L_{\mathrm{sf}}}\left(z - \frac{L_d + L_w}{2}\right) \tag{13}$$

and dimensionless variables

$$\bar{\alpha}(\bar{z}) = \begin{cases} \alpha(z)/\mu_{\mathrm{sf}}, & \alpha \in \{\mu_n, \mu_p\} \\ \alpha(z)/\phi_{\mathrm{sf}}, & \alpha \in \{\phi, \phi_n, \phi_p, V_{\mathrm{ext}}\} \\ \alpha(z)/\mathrm{E}_{\mathrm{sf}}, & \alpha \in \{\chi, \mathrm{E}_{0,c,F_n,F_p,g,i,v}\} \\ \alpha(z)/N_{\mathrm{sf}}, & \alpha \in \{n, p, n_i, N_{0,c,D,f,v}\} \\ \alpha(z)/G_{\mathrm{sf}}, & \alpha \in \{G, R\} \\ \alpha(z)/J_{\mathrm{sf}}, & \alpha \in \{J_n, J_p\} \end{cases}, \tag{14}$$

where

$$\left.\begin{aligned} &L_{\mathrm{sf}} = (L_d - L_w)/2, && \mu_{\mathrm{sf}} = (1/2)\max\{\mu_n(z) + \mu_p(z)\} \\ &\phi_{\mathrm{sf}} = k_B T/q_e, && \mathrm{E}_{\mathrm{sf}} = k_B T \\ &N_{\mathrm{sf}} = \max\{N_f(z) + N_D(z)\}, && G_{\mathrm{sf}} = \mu_{\mathrm{sf}} N_{\mathrm{sf}} \phi_{\mathrm{sf}}/L_{\mathrm{sf}}^2 \\ &J_{\mathrm{sf}} = q_e G_{\mathrm{sf}} L_{\mathrm{sf}} \end{aligned}\right\} \tag{15}$$

are the scale factors. We also define the dimensionless z-directed d.c. electric field

$$\bar{E}_{\mathrm{dc}}(\bar{z}) = -\lambda^2(\bar{z})\frac{d}{d\bar{z}}\bar{\phi}(\bar{z}) \tag{16}$$

along with the Poisson function

$$\lambda^2(\bar{z}) = \varepsilon_0\varepsilon_{\mathrm{dc}}(z)\frac{k_B T}{(q_e L_{\mathrm{sf}})^2 N_{\mathrm{sf}}}. \tag{17}$$

After non-dimensionalization, Eqs. (10a)–(10d), (12a), and (12b) can be manipulated to yield

$$\bar{n}(\bar{z}) = \exp\left[\bar{\Phi}_n + \bar{\mathrm{E}}_{F_n}(\bar{z}) + \bar{\phi}(\bar{z}) + \bar{\phi}_n(\bar{z})\right] \tag{18a}$$

and

$$\bar{p}(\bar{z}) = \exp\left[\bar{\Phi}_p - \bar{\mathrm{E}}_{F_p}(\bar{z}) - \bar{\phi}(\bar{z}) - \bar{\phi}_p(\bar{z})\right], \tag{18b}$$

where $\bar{\Phi}_n = \ln \bar{N}_0 + \bar{\mathrm{E}}_0$ and $\bar{\Phi}_p = \ln \bar{N}_0 - \bar{\mathrm{E}}_0$ are arbitrary dimensionless constants. By choosing $\bar{\mathrm{E}}_{F_n}(\bar{z})$ and $\bar{\mathrm{E}}_{F_p}(\bar{z})$ as the dependent variables in the new algorithm, in contrast to the choice of $\bar{n}(\bar{z})$ and $\bar{p}(\bar{z})$ as dependent variables in the algorithm used for Part I [13], we avoid the unphysical possibility of negative carrier densities.

After non-dimensionalization and consistently with the Boltzmann approximation, Eqs. (6)–(9) and (16) transform into three coupled sets of two ordinary differential equations for $\bar{z} \in (-1, 1)$, the two equations in each set being

$$\frac{d}{d\bar{z}}g(\bar{z}) = f(\bar{z}) \tag{19a}$$

and

$$\frac{d}{d\bar{z}}w(\bar{z}) = \frac{g(\bar{z})}{u(\bar{z})}. \tag{19b}$$

The choices of functions $g(\bar{z})$, $f(\bar{z})$, $u(\bar{z})$, and $w(\bar{z})$ for each of the three sets are given in Table 1.

We now describe the numerical implementation of the new algorithm for the electrical submodel. A one-dimensional mesh $\{\bar{z}_j\}_{j=0}^{N}$ is defined on the domain $\Omega = \{\bar{z} | -1 \le \bar{z} \le 1\}$ such that $\bar{z}_0 = -1$ and $\bar{z}_N = 1$. The mesh midpoints we define as $\bar{z}_{j+1/2} = 2^{-1}(\bar{z}_j + \bar{z}_{j+1})$. We allow this mesh to be graded, with mesh size

$$h_j = \bar{z}_{j+1} - \bar{z}_j \quad (j = 0, \cdots, N-1). \tag{20}$$

Clearly, $g(\bar{z})$ must be continuous $\forall \bar{z} \in (-1, 1)$. Otherwise, the right side of Eq. (19a)—i.e., $f(\bar{z})$—would involve Dirac delta functions. Therefore, we choose the approximate numerical solution such that

(i) $g(\bar{z})$ is piecewise linear, and
(ii) $u(\bar{z})$, $w(\bar{z})$, and $f(\bar{z})$ are piecewise constant

Table 1. Choice of Variables for the FDM Algorithm

Set No.	Unknown	Choice
1	$w = \bar{\mathrm{E}}_{F_n}(\bar{z})$	$u = \bar{\mu}_n(\bar{z})\bar{n}(\bar{z})$
	$g = \bar{J}_n(\bar{z})$	$f = -\bar{G}(\bar{z}) + \bar{R}(\bar{n}, \bar{p}; \bar{z})$
2	$w = \bar{\mathrm{E}}_{F_p}(\bar{z})$	$u = \bar{\mu}_p(\bar{z})\bar{p}(\bar{z})$
	$g = \bar{J}_p(\bar{z})$	$f = \bar{G}(\bar{z}) - \bar{R}(\bar{n}, \bar{p}; \bar{z})$
3	$w = \bar{\phi}(\bar{z})$	$u = -\lambda^2(\bar{z})$
	$g = \bar{E}_{\mathrm{dc}}(\bar{z})$	$f = \bar{n}(\bar{z}) - \bar{p}(\bar{z}) - \bar{N}_f(\bar{z}) - \bar{N}_D(\bar{z})$

in Ω. We adopt the following notion: $g_j = g(\bar{z}_j)$, $u_{j+1/2} = u(\bar{z}_{j+1/2})$, $w_{j+1/2} = w(\bar{z}_{j+1/2})$, and $f_{j+1/2} = f(\bar{z}_{j+1/2})$.

We allow $\bar{\phi}_{n,p}(\bar{z})$ and $\bar{\mu}_{n,p}(\bar{z})$ to have jumps across nodes $\bar{z}_k$. Therefore, at these nodes we weakly enforce the continuity of the quasi-Fermi potentials

$$\left[\left[\bar{\mathrm{E}}_{F_\ell}\right]\right]_{z=z_k} = \bar{\mathrm{E}}^{+}_{F_\ell}(\bar{z}_k) - \bar{\mathrm{E}}^{-}_{F_\ell}(\bar{z}_k) = 0 \quad (\ell = n, p), \tag{21}$$

where the superscript + denotes the limit from above to $\bar{z}_k$, and the superscript - denotes the limit from below to $\bar{z}_k$. This is done by deriving an integral representation for the quasi-Fermi potential $\bar{\mathrm{E}}_{F_p}$ (similarly for $\bar{\mathrm{E}}_{F_n}$) in the following way.

After defining the Scharfetter–Gummel integrating factor for holes as

$$\bar{M}_p(\bar{z}) = \exp\left[\bar{\phi}(\bar{z}) + \bar{\phi}_p(\bar{z})\right], \tag{22}$$

we get

$$\bar{M}_p(\bar{z})\bar{J}_p(\bar{z}) = -\bar{\mu}_p(\bar{z})\frac{d}{d\bar{z}}\left\{\exp\left[\bar{\Phi}_p - \bar{\mathrm{E}}_{F_p}(\bar{z})\right]\right\} \tag{23}$$

from Eq. (11b). In order to formulate the new algorithm, we use an integral form of Eq. (23), which differs from Eq. (10b) in that it is written in terms of integrals of the current density $\bar{J}_p$ rather than the hole density $\bar{p}$. After dividing both sides by $\bar{\mu}_p(\bar{z})$ and integrating, the exact quasi-Fermi potential for holes away from the midpoint of the mesh interval can be represented as

$$\bar{E}_{F_p}(\bar{z}) = \bar{\Phi}_p - \ln\left\{-\int_{\bar{z}_{j+1/2}}^{\bar{z}} \frac{\bar{M}_p(\tau)\bar{J}_p(\tau)}{\bar{\mu}_p(\tau)}\,\mathrm{d}\tau + \exp\left[\bar{\Phi}_p - \bar{\mathrm{E}}_{F_p,j+1/2}\right]\right\} \tag{24}$$

in Ω. This form of Eq. (23) shows how the quasi-Fermi potential depends on the current density. We now discretize the right side of Eq. (24) by imposing the approximation that both $\bar{M}_p(\bar{z})$ and $\bar{\mu}(\bar{z})$ are constant on each mesh interval while $\bar{J}_p(\bar{z})$ is piecewise linear. We apply this integral representation for $\bar{\mathrm{E}}_{F_p}(\bar{z})$ on the intervals $[\bar{z}_{k-1/2}, \bar{z}_k]$ and $[\bar{z}_k, \bar{z}_{k+1/2}]$ to find $\bar{\mathrm{E}}^{+}_{F_p,k}$ and $\bar{\mathrm{E}}^{-}_{F_p,k}$, respectively. By our assumptions, the integrand in each expression is piecewise linear, and we can compute these integrals without any additional loss of accuracy. After using Eq. (21), the jump resulting condition for $\bar{\mathrm{E}}_{F_p}(\bar{z})$ is

$$-\frac{\bar{M}_{p,k-1/2}}{\bar{\mu}_{p,k-1/2}}\frac{(\bar{J}_{p,k-1} + 3\bar{J}_{p,k})}{8}h_{k-1} + \exp\left(\bar{\Phi}_p - \bar{\mathrm{E}}_{F_p,k-1/2}\right) = -\frac{\bar{M}_{p,k+1/2}}{\bar{\mu}_{p,k+1/2}}\frac{(\bar{J}_{p,k+1} + 3\bar{J}_{p,k})}{8}h_k + \exp\left(\bar{\Phi}_p - \bar{\mathrm{E}}_{F_p,k+1/2}\right) \tag{25}$$

at node $\bar{z}_k$. The jump condition for $\bar{\mathrm{E}}_{F_n}(\bar{z})$ at node $\bar{z}_k$ is enforced in a similar way. The electric potential $\bar{\phi}(\bar{z})$ does not have jumps.

Now we let

$$\Gamma_j(\bar{z}) = \begin{cases} 0, & \bar{z} \notin [\bar{z}_j, \bar{z}_{j+1}] \\ 1, & \bar{z} \in [\bar{z}_j, \bar{z}_{j+1}] \end{cases} \tag{26}$$

be a test function. Multiplying Eq. (19a) by $\Gamma_j(\bar{z})$ and integrating over $\bar{z} \in [\bar{z}_j, \bar{z}_{j+1}]$, we get

$$\frac{g_{j+1} - g_j}{h_j} = f_{j+1/2} \quad (j = 0, \cdots, N-1). \tag{27}$$

Next we take a piecewise linear test function Ξ_j that vanishes at $\bar{z} = \pm 1$ as well as $\forall\, \bar{z} < \bar{z}_{j-1}$ and $\forall\, \bar{z} > \bar{z}_{j+1}$, but equals unity at $\bar{z} = \bar{z}_j$. We divide Eq. (19b) through by u, multiply by Ξ_j, and integrate by parts over Ω. Using the trapezoidal rule for integration [47] to approximate the resulting integral, we get

$$g_j = H_j(u)\big(w_{j+1/2} - w_{j-1/2}\big) \quad (j = 1, \ldots, N-1) \tag{28}$$

for $j \neq k$, where

$$H_j(u) = \frac{2}{\left(\frac{h_j}{u_j^+} + \frac{h_{j-1}}{u_j^-}\right)} \tag{29}$$

is the harmonic average of u/h at node $\bar{z}_j$. We choose to take $u_j^+ = u_{j+1/2}$ and $u_j^- = u_{j-1/2}$.

At a boundary node where either $j = 0$ or $j = N$, we again use the integral representations of $\bar{\mathrm{E}}_{F_n}(\bar{z})$ and $\bar{\mathrm{E}}_{F_p}(\bar{z})$ to find $\bar{\mathrm{E}}_{F_n,1/2}$, $\bar{\mathrm{E}}_{F_p,1/2}$, $\bar{\mathrm{E}}_{F_n,N-1/2}$, and $\bar{\mathrm{E}}_{F_p,N-1/2}$. For example, we find

$$\bar{J}_{p,1} + 3\bar{J}_{p,0} = -\frac{8\bar{\Phi}_p \bar{\mu}_{p,1/2}}{h_0 \bar{M}_{p,1/2}}\left[\exp\left(-\bar{\mathrm{E}}_{F_p,0}\right) - \exp\left(-\bar{\mathrm{E}}_{F_p,1/2}\right)\right]. \tag{30}$$

On the other hand, setting $g = \bar{J}_p$ and $j = 0$ in Eq. (27) and adding $4\bar{J}_{p,0}/h_0$ to both sides gives

$$\bar{J}_{p,1} + 3\bar{J}_{p,0} = h_0 f_{1/2} + 4\bar{J}_{p,0}. \tag{31}$$

The previous two expressions together yield

$$\bar{J}_{p,0} = -\frac{2\bar{\Phi}_p \bar{\mu}_{p,1/2}}{h_0 \bar{M}_{p,1/2}}\left[\exp\left(-\bar{\mathrm{E}}_{F_p,0}\right) - \exp\left(-\bar{\mathrm{E}}_{F_p,1/2}\right)\right] - \frac{h_0 f_{1/2}}{4}. \tag{32}$$

In a similar way, we can find expressions for $\bar{J}_{p,N}$, $\bar{J}_{n,0}$, and $\bar{J}_{n,N}$.

The FDM requires the solution of the $3N$ equations given by Eqs. (27), (28), and (32) along with the jump conditions exemplified by Eq. (25). We define the $(N \times 1)$ column vectors

$$\boldsymbol{w} = \left[\, w_{1/2}, w_{3/2}, \ldots, w_{N-1/2}\right]^T, \tag{33}$$

$\boldsymbol{w} \in \{\bar{\boldsymbol{E}}_{F_n}, \bar{\boldsymbol{E}}_{F_p}, \bar{\boldsymbol{\phi}}\}$ and the $(3N \times 1)$ vector $\boldsymbol{x} = [\bar{\boldsymbol{E}}_{F_n}^T, \bar{\boldsymbol{E}}_{F_p}^T, \bar{\boldsymbol{\phi}}^T]^T$. Using MATLAB version R2021b, we solve the $3N$ equations $F(\boldsymbol{x}) = 0$ using a Newton method and continuation using selected damped electromagnetic parameters [48]. Once $\boldsymbol{x}$ has been found, the current densities $\bar{J}_n(\bar{z})$ and $\bar{J}_p(\bar{z})$ can be calculated using Eq. (27). Also, $\bar{n}(\bar{z})$ and $\bar{p}(\bar{z})$ can be recovered using Eqs. (18a) and (18b), respectively. Each Newton solution process terminates when the relative L^2 norm of the residual is less than 10^{-10}. Initially, we set $\bar{\Phi}_n = 1$ and $\bar{\Phi}_p = 1$; thereafter, at each step of the damped Newton method, the constants $\bar{\Phi}_n$ and $\bar{\Phi}_p$ are updated using the latest values of $\bar{n}$ and $\bar{p}$.

Material data required by the electrical submodel are available in Part I [13], with the following difference. The defect density N_f reported in Part I [13] had been modeled as a linear function of ξ. With the normalization error removed, the nonlinear fit shown in Fig. 2 had to be used to match the experimental data adequately. In this figure, N_f is independent of $\xi \in [0, 0.3]$ but a quadratic function of $\xi \in [0.55, 1]$. This nonlinear fit was used for all results reported in Section 3.

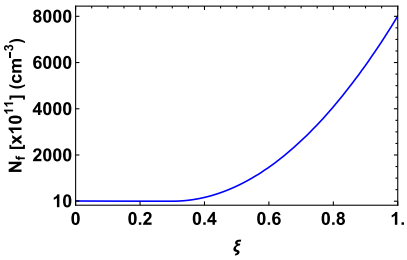

Fig. 2. Defect density N_f as a function of ξ used for the new algorithm.

Testing was performed comparing the high-order corrected HDG scheme of Part I with our new FDM scheme for models and parameters where both solvers converge, in order to ensure that the latter scheme reproduces results obtained with the former scheme.

E. Optoelectronic Optimization

Solution of the drift-diffusion system yields the device current density

$$J_{\mathrm{dev}} = J_n(z) + J_p(z), \tag{34}$$

which is independent of z but is a function of V_{ext}. The product $P = J_{\mathrm{dev}} V_{\mathrm{ext}}$ can then be maximized by varying V_{ext} to obtain the maximum power that the solar cell can produce and hence the efficiency η for any particular design. The design of the solar cell can then be improved using the differential evolution algorithm [49] to determine the design with the highest efficiency as in Part I [13].

3. NUMERICAL RESULTS AND DISCUSSION

A. Conventional CIGS Solar Cell (Model Validation)

First, we validated our coupled optoelectronic model solved using the FDM by comparison with extant experimental results for the conventional MgF_2/AZO/od–ZnO/CdS/CIGS/Mo solar cell containing a 2200-nm-thick homogeneous CIGS layer and a flat backreflector [50]. Values of J_{sc}, V_{oc}, FF, and η obtained from our model for $\xi = 0$ ($\mathrm{E}_g = 0.947$ eV), $\xi = 0.25$ ($\mathrm{E}_g = 1.12$ eV), and $\xi = 1$ ($\mathrm{E}_g = 1.626$ eV) are provided in Table 2, as also are the corresponding experimental data [50,51]. The model predictions are in reasonable agreement with the experimental data, the differences very likely due to variance between the optical and electrical properties used in the model from those realized in practice.

B. Optimal Solar Cell with Homogeneous Bandgap

Next, let us consider the optoelectronic optimization of η for fixed values of L_{CIGS} for a solar cell with a homogeneous-bandgap photon-absorbing layer. The parameter space for optimizing η was set to: $\mathrm{E}_{g,\min} \in [0.947, 1.626]$ eV. Values of J_{sc},

Table 2. Comparison of J_{sc}, V_{oc}, FF, and η Predicted by the Coupled Optoelectronic Model for a Conventional CIGS Solar Cell with a Homogeneous CIGS Layer (i.e., $A = 0$) with Their Experimental Counterparts [50,51]

ξ	$E_{g,min}$ (eV)		J_{sc} (mA cm^{-2})	V_{oc} (mV)	FF (%)	η (%)
0	0.95	Model	37.79	460	79.32	13.79
		Experiment (Ref. [50])	40.58	491	66	14.5
		Experiment (Ref. [50])	41.10	491	75	15.0
0.25	1.12	Model	33.95	630	82	17.64
		Experiment (Ref. [50])	35.22	692	79	19.50
		Experiment (Ref. [51])	37.8	741	81	22.60
1	1.626	Model	14.78	1030	70	10.66
		Experiment (Ref. [50])	14.88	823	71	9.53
		Experiment (Ref. [50])	18.61	905	75	10.20

Table 3. Predicted Parameters of the Optimal CIGS Solar Cell with a Specified Value of $L_{CIGS} \in [100, 2200]$ nm, When the CIGS Layer Is Homogeneous ($E_{g,min} \in [0.947, 1.626]$ eV and $A = 0$)

L_{CIGS} (nm)	$E_{g,min}$ (eV)	J_{sc} (mA cm^{-2})	V_{oc} (mV)	FF (%)	η (%)
100	1.33	14.55	680	78	7.78
200	1.31	19.53	710	76	10.57
300	1.28	22.99	710	76	12.53
400	1.28	24.16	720	77	13.55
500	1.27	24.92	720	79	14.18
600	1.26	26.09	720	79	14.94
900	1.26	27.35	730	81	16.20
1200	1.25	28.43	730	81	16.96
2200	1.19	31.86	700	82	18.39

V_{oc}, FF, and η corresponding to the optimal design for $L_{CIGS} \in \{100, 200, 300, 400, 500, 600, 900, 1200, 2200\}$ nm are shown in Table 3. As L_{CIGS} increases from 100 to 2200 nm, the optimal value of E_g monotonically decreases from 1.33 to 1.19 eV, and the optimal efficiency increases steadily from 7.78% to 18.39%. The highest efficiency predicted is 18.39%, for a solar cell with a 2200-nm-thick CIGS layer with an optimal bandgap of $E_g = 1.19$ eV.

C. Optimal Solar Cell with Linear Bandgap Grading

Next, let us consider the maximization of η as a function of L_{CIGS} when the CIGS layer has a linearly graded bandgap, according to either Eq. (1) or Eq (2).

1. Forward Grading

Equation (1) was used for linearly nonhomogeneous forward bandgap grading, so that $E_g(L_w + L_{od-ZnO} + L_{CdS}) \le E_g(L_d)$ for $A \ge 0$, the bandgap being smaller near the front contact than near the back contact. The optoelectronic optimization predicts $A > 0$ for optimal efficiency, contrary to the prediction in Part I [13] due to the normalization error mentioned previously. Values of J_{sc}, V_{oc}, FF, and η corresponding to the optimal design for $L_{CIGS} \in \{100, 200, 300, 400, 500, 600, 900, 1200, 2200\}$ nm are shown in Table 4.

For $L_{CIGS} = 2200$ nm, the optimal $\eta = 24.17\%$ in Table 4, whereas $\eta = 18.39\%$ in Table 3. This relative enhancement of 31.43% must be attributed to the forward bandgap grading of the CIGS layer. Concurrently, J_{sc} increases from 31.86 to 36.38 mA cm^{-2} (14.18% relative increase) and V_{oc} from 700 to 810 mV (15.71% relative increase); however, the fill factor remains the same. Bandgap grading thus calls for large $E_g(z)$ in the proximity of the plane $z = L_d$, which elevates V_{oc}. Also, in the vicinity of the CdS/CIGS interface, $E_g(z)$ is small and therefore elevates the EHP generation rate [52]. The overall trends remain the same as reported in Part I [13].

Table 4. Predicted Parameters of the Optimal CIGS Solar Cell with a Specified Value of $L_{CIGS} \in [100, 2200]$ nm, When the CIGS Layer Is Linearly Nonhomogeneous According to Eq. (1)

L_{CIGS} (nm)	$E_{g,min}$ (eV)	$E_{g,max}$ (eV)	A	J_{sc} (mA cm^{-2})	V_{oc} (mV)	FF (%)	η (%)
100	0.96	1.52	0.99	14.99	840	82	10.29
200	0.96	1.62	0.98	21.51	910	79	15.55
300	0.96	1.62	0.98	24.49	900	80	17.55
400	0.96	1.62	0.98	27.19	890	80	19.32
500	0.95	1.62	0.99	28.61	880	80	20.17
600	0.95	1.62	0.98	30.02	870	80	21.01
900	0.95	1.62	0.99	32.61	850	81	22.49
1200	0.95	1.62	0.98	34.01	840	81	23.18
2200	0.95	1.62	0.98	36.38	810	82	24.17

2. Backward Grading

Equation (2) was used for linearly forward bandgap grading so that $E_g(L_w + L_{od-ZnO} + L_{CdS}) \ge E_g(L_d)$ for $A \ge 0$. Optoelectronic optimization yielded $A = 0$. Thus, Table 3 holds for forward bandgap grading of the CIGS layer, again in contrast to Part I [13], no doubt as a result of the normalization error in the electrical-submodel code.

D. Optimal Solar Cell with Nonlinear Bandgap Grading

Next, let us consider the optoelectronic optimization of η for fixed values of L_{CIGS} for a solar cell with a nonhomogeneous CIGS layer graded according to Eq. (3). Values of η optimized for fixed L_{CIGS} are shown in Table 5. Values of $E_{g,min}$, A, α, K, ψ, J_{sc}, V_{oc}, and FF for each optimal design are also shown in this table.

Table 5. Predicted Parameters of the Optimal CIGS Solar Cell with a Specified Value of $L_{CIGS} \in [100, 2200]$ nm, When the CIGS Layer Is Nonlinearly Graded According to Eq. (3)

L_{CIGS} (nm)	$E_{g,min}$ (eV)	A	α	K	ψ	J_{sc} (mA cm^{-2})	V_{oc} (mV)	FF (%)	η (%)
100	1.07	1.0	8	0.60	0.36	17.10	950	87	14.10
200	1.07	1.0	8	0.60	0.36	23.74	970	87	19.98
300	1.07	1.0	8	0.60	0.36	27.49	980	86	23.28
400	1.07	1.0	8	0.60	0.36	30.06	990	86	25.45
500	1.07	1.0	8	0.60	0.36	32.01	990	85	27.04
600	1.07	1.0	8	0.60	0.36	32.78	990	85	27.56
900	1.07	1.0	8	0.60	0.36	35.36	1000	83	29.32
1200	1.07	1.0	8	0.60	0.36	36.36	1000	82	29.74
2000	1.07	1.0	8	0.60	0.36	37.84	990	80	30.03
2200	1.07	1.0	8	0.60	0.36	38.02	980	80	29.98

The highest optimal $\eta = 30.03\%$ in Table 5 was obtained with the 2000-nm-thick CIGS layer, a relative enhancement of 63.29% with respect to $\eta = 18.39\%$ with the homogeneous CIGS layer in Table 3. The short-circuit current density increases from 31.86 mA cm^{-2} by 18.76% to 37.84 mA cm^{-2}, and the open-circuit voltage increases from 700 mV by 41.42% to 990 mV, but the fill factor reduces to 82% from 80%.

The overall trend is the higher efficiency with nonlinear grading of CIGS photon-absorbing layer compared to either homogeneous bandgap (Section 3.B) or linearly graded bandgap (Section 3.C). In general, this trend remains the same as reported in Part I [13].

E. Detailed Study of Optimal Solar Cells with 600-nm-Ultrathin CIGS Layer

The highest efficiency reported in Tables 3–5 is 30.03%. This is for the CIGS solar cell with a nonlinearly graded-bandgap 2000-nm-thick CIGS layer. However, we are interested in ultrathin CIGS layers to reduce the material and processing costs, keeping in mind the scarcity of indium. According to a cost analysis published by the US National Renewable Energy Laboratory [53], 25% of the module cost is only due to the CIGS layer. Reducing the thickness of this layer by two-thirds will possibly reduce the overall cost by as much as 8%. The solar cell with the nonlinearly graded-bandgap CIGS layer of 600 nm thickness has efficiency $\eta = 27.56\%$, which is significantly more than the efficiency of the conventional CIGS solar cell with a 2200-nm-thick homogeneous CIGS layer [51]. Therefore, as in Part I [13], a detailed study of the solar cell with the 600-nm-thick graded-bandgap/nonhomogeneous CIGS absorber layer is reported next.

1. Forward Linearly Graded-Bandgap CIGS Layer

The design and performance parameters of the optimal CIGS solar cell with a 600-nm-thick linearly graded-bandgap CIGS layer are provided in Table 4. Spatial profiles of $E_g(z)$ and $\chi(z)$ delivered by optoelectronic optimization are provided in Figs. 3(a) and 3(b), respectively. Spatial profiles of $E_c(z)$, $E_v(z)$, and the intrinsic energy $E_i(z)$ are presented in Fig. 3(c). The spatial variations of E_v and E_i are similar to that of E_g, as also in Part I [13]. Figure 3(d) presents the spatial profiles of $n(z)$, $p(z)$, and $n_i(z)$ under the equilibrium condition. The intrinsic carrier density varies linearly with ξ, such that it is small where E_g is large and vice versa.

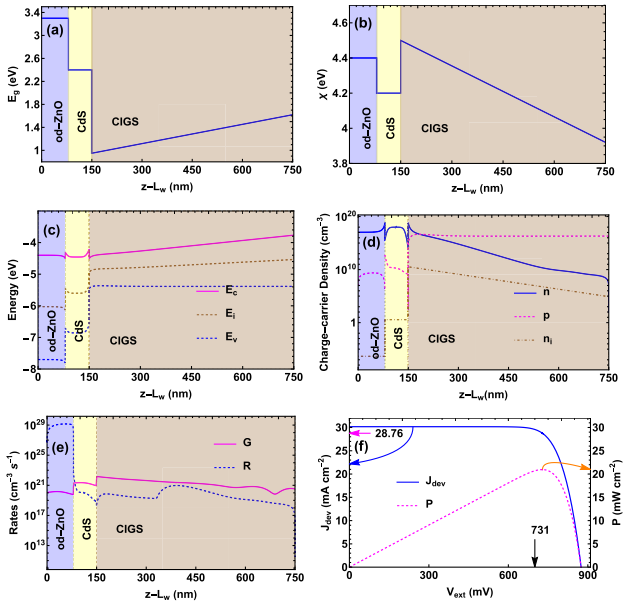

Fig. 3. (a) Spatial profiles of (a) E_g; (b) χ; (c) $E_c(z)$, $E_v(z)$, and $E_i(z)$; (d) $n(z)$, $p(z)$, and $n_i(z)$; and (e) $G(z)$ and $R(n, p; z)$ in the od-ZnO/CdS/CIGS region of the optimal CIGS solar cell with a 600-nm-thick linearly graded-bandgap CIGS layer. (f) Plots of J_{dev} and P versus V_{ext} for the same solar cell.

Spatial profiles of $G(z)$ and $R(n, p; z)$ are given in Fig. 3(e). The generation rate is higher near the front face $z = L_w + L_{od\text{–}ZnO} + L_{CdS}$ and slightly lower in the middle of the CIGS layer, but the recombination rate drops sharply near the back face of that layer. The $J_{dev}-V_{ext}$ characteristics of the solar cell are shown in Fig. 3(f). From this figure, $J_{dev} = 28.76$ mA cm^{-2}, $V_{ext} = 731$ mV, FF = 80%, and $\eta = 21.01\%$ for the best performance.

2. Nonlinearly Graded-Bandgap CIGS Layer

The parameters of the optimal CIGS solar cell with a 600-nm-thick nonlinearly graded-bandgap CIGS layer are provided in Table 5. Spatial profiles of $E_g(z)$ and $\chi(z)$ delivered by optoelectronic optimization are provided in Figs. 4(a) and 4(b), respectively, and those of $E_c(z)$, $E_v(z)$, and $E_i(z)$ in Fig. 4(c).

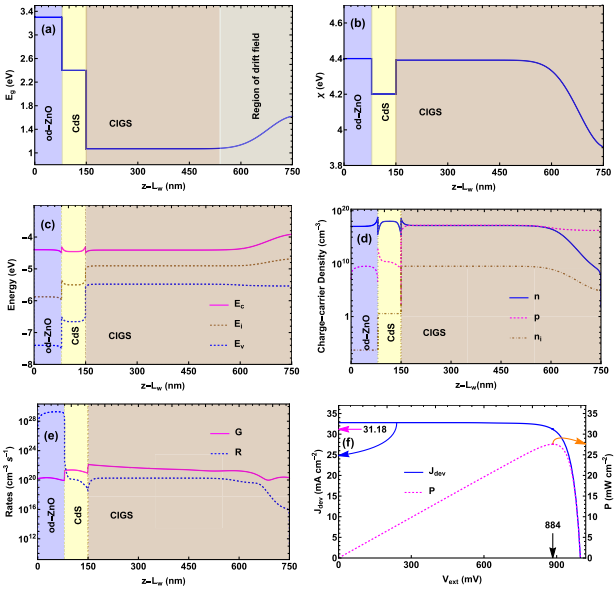

Fig. 4. (a) Spatial profiles of (a) E_g; (b) χ; (c) $\mathrm{E}_c(z)$, $\mathrm{E}_v(z)$, and $\mathrm{E}_i(z)$; (d) $n(z)$, $p(z)$, and $n_i(z)$; and (e) $G(z)$ and $R(n, p; z)$ in the od-ZnO/CdS/CIGS region of the optimal CIGS solar cell with a 600-nm-thick nonlinearly graded bandgap CIGS layer. (f) Plots of J_{dev} and P versus V_{ext} for the same solar cell.

The spatial variations of E_v and E_i are similar to that of E_g and provide the conditions to enhance the EHP generation rate, and bandgap grading provides the condition of large $\mathrm{E}_g(z)$ in the proximity of the plane $z = L_d$, which elevates V_{oc} [52], these characteristics being the same as reported in Part I [13]. Figure 4(d) presents the graphs of $n(z)$, $p(z)$, and $n_i(z)$ under the equilibrium condition. The intrinsic carrier density varies according to the bandgap variation such that it is small where E_g is large and vice versa, just as in Part I [13].

Spatial profiles of $G(z)$ and $R(n, p; z)$ are given in Fig. 4(e). The magnitude of $\mathrm{E}_g(z)$ is large in the proximity of the back plane $z = L_d$, which elevates V_{oc}. The regions in which $\mathrm{E}_g(z)$ is small are of substantial thickness, these regions being responsible for elevating the EHP generation rate [52]. The nonlinear grading close to the back plane $z = L_d$ [shown in Fig. 4(a)] adds a drift field to reduce the back-surface EHP recombination rate, supplementing the role of the Al_2O_3 passivation layer. Furthermore, the spatial profile of the EHP recombination rate follows that of the defect density N_{t}. These trends are the same as in Part I [13].

The $J_{\mathrm{dev}} - V_{\mathrm{ext}}$ characteristics of the solar cell are shown in Fig. 4(f). From this figure, $J_{\mathrm{dev}} = 31.18\ \mathrm{mA\,cm^{-2}}$, $V_{\mathrm{ext}} = 884\ \mathrm{mV}$, FF = 85%, and $\eta = 27.56\%$ for the best performance.

F. Illumination by Concentrated Sunlight

Large gains in efficiency can arise because bandgap grading can provide a way to capture solar photons in a wider spectral regime, which is also the principle exploited in multi-junction III-V solar cells. Moreover, bandgap grading offers the additional benefits of a higher open-circuit voltage and reduced parasitic impedances, without the additional circuitry needed for multi-junction solar cells [54]. Hence, sunlight concentration combined with bandgap grading of thin-film solar cells may offer a cost-effective alternative to III-V multi-junction solar cells.

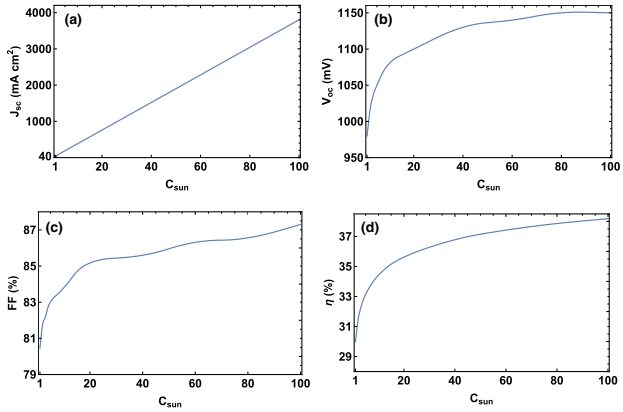

Fig. 5. Plots of (a) J_{sc}, (b) V_{oc}, (c) η, and (d) FF of the optimal thin-film solar cell with a nonlinearly graded-bandgap CIGS layer of 2200 nm thickness as functions of c_{sun}.

Sunlight concentration can be achieved using optical light collectors, such as lenses or mirrors [55]. The sunlight-concentration factor is defined as the number c_{sun} of suns, the single-sun spectrum $S(\lambda_0)$ being replaced by $c_{\mathrm{sun}} S(\lambda_0)$ in Eq. (5). Since the thickness of thin-film solar cells is on the order of a few micrometers, $c_{\mathrm{sun}} \in [1, 100]$ was restricted to be of medium magnitude in order to avoid detrimental heating effects [28].

1. Optimal Solar Cell

Next, we examined the performance of the optimal solar cell with a nonlinearly graded-bandgap CIGS layer of 2200 nm thickness (with parameters provided in the last row of Table 5), when exposed to concentrated sunlight. Plots of J_{sc}, V_{oc}, η, and FF of the optimal solar cell as functions of the sunlight-concentration factor $c_{\mathrm{sun}} \in [1, 100]$ are shown in Fig. 5. The maximum value of η predicted is 38.18% with $c_{\mathrm{sun}} = 100$. The 100-sun efficiency is 127.35% of the one-sun efficiency (29.98%). The 100-sun values of J_{sc}, V_{oc}, and FF are $3802\ \mathrm{mA\,cm^{-2}}$, 1150 mV, and 87%, respectively.

The linear relationship of J_{sc} with c_{sun} is evident in Fig. 5(a). In contrast, V_{oc}, η, and FF in Figs. 5(b)–5(d) evince a two-phase trend: as c_{sun} increases from 1 to 100, each of these three parameters increases linearly: at a high rate in the first phase, but at a much slower rate in the second phase. The same trends had been reported earlier [28], which however had suffered from a normalization error in the electrical-submodel code.

The $J_{\mathrm{dev}} - V_{\mathrm{ext}}$ and $P - V_{\mathrm{ext}}$ characteristics of the optimal CIGS thin-film solar cell are shown in Fig. 6 for $c_{\mathrm{sun}} = 100$. The maximum output power P_{max} delivered is $38.18\ \mathrm{mW\,cm^{-2}}$ for $c_{\mathrm{sun}} = 100$. Of course, the ratio $P_{\mathrm{max}}/c_{\mathrm{sun}}$ increases by 27.35% with hundredfold sunlight concentration, as is expected from the increase of η by the same factor. From this figure, $J_{\mathrm{dev}} = 3671\ \mathrm{mA\,cm^{-2}}$, $V_{\mathrm{ext}} = 1040\ \mathrm{mV}$, FF = 87%, and $\eta = 38.18\%$ for the best performance.

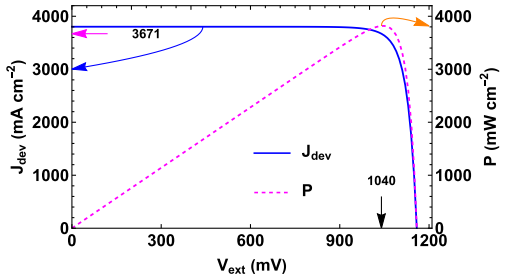

Fig. 6. Plots of J_{dev} and P vs. V_{ext} of the optimal thin-film solar cell with a nonlinearly graded-bandgap CIGS layer of 2200 nm thickness when $c_{sun} = 100$.

2. Effect of Sunlight Concentration on Generation/Recombination Processes

We also examined the spatial profiles of the c_{sun}-sun EHP generation rate $G_{c_{sun}}(z)$ and the c_{sun}-sun EHP recombination rate $R_{c_{sun}}(n, p; z)$ in order to determine which portions of the semiconductor region are responsible for efficiency enhancement from sunlight concentration. We also determined the values of the net generation rate

$$\gamma_{c_{sun}} = \int_{L_d}^{L_w} G_{c_{sun}}(z)\mathrm{d}z \tag{35a}$$

and the net recombination rate

$$\rho_{c_{sun}} = \int_{L_d}^{L_w} R_{c_{sun}}(n, p; z)\mathrm{d}z. \tag{35b}$$

The EHP generation rates $G_{100}(z)$ and $100G_1(z)$ are plotted in Fig. 7(a) as functions of z in the semiconductor region of the optimal thin-film solar cell with a nonlinearly graded-bandgap CIGS layer of 2200 nm thickness. The plots show that $G_{100}(z) = 100G_1(z)$, as expected from the linearity of the optical submodel. Not surprisingly, therefore, $\gamma_{100} = 100\gamma_1 = 2.43 \times 10^{26}\ \mathrm{cm^{-2}\ s^{-1}}$.

Both $R_{100}(n, p; z)$ and $100R_1(n, p; z)$ are plotted as functions of z in the semiconductor regions of the same solar cell in Fig. 7(b). Clearly, $R_{100}(n, p; z) \neq 100R_1(n, p; z)$. Indeed, $R_{100}(n, p; z) < 100R_1(n, p; z)$ in most of the CIGS layer, but the per-sun recombination rate near the two faces of that layer is affected very little by sunlight concentration. In consequence of $100R_1(n, p; z)$ exceeding $R_{100}(n, p; z)$ in most of the CIGS layer, $100\rho_1 = 5.295 \times 10^{24}\ \mathrm{cm^{-2}\ s^{-1}}$ is about 1% higher than $\rho_{100} = 5.257 \times 10^{24}\ \mathrm{cm^{-2}\ s^{-1}}$, which shows that the reduced per-sun recombination rate is a significant reason for the efficiency enhancement in the CIGS solar cell on exposure to concentrated sunlight. Another reason includes the

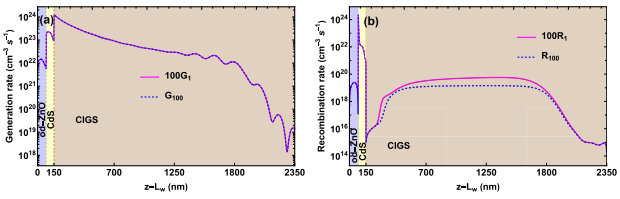

Fig. 7. Spatial profiles of (a) the EHP generation rate and (b) the EHP recombination rate in the semiconductor region of the optimal solar cell with a nonlinearly graded-bandgap CIGS layer of 2200 nm thickness, for the one-sun and 100-sun illumination conditions.

improvement of V_{oc} due to higher J_{sc}, as it is proportional to $\ln(1 + J_{sc}/J_{dark})$ for ideal photodiodes, where J_{dark} is the dark current density; see Eq. (1.6) of Ref. [56].

G. CIGS Solar Cell with Optimal SLARC/DLARC

The structure for CIGS solar cell with a DLARC is shown in Fig. 1(c). We optimized the refractive indices (n_1 and n_2) and thicknesses (L_{ARC1} and L_{ARC2}) of a DLARC for optimal solar cells containing a CIGS photon-absorbing layer with

(i) homogeneous bandgap and 2200 nm thickness,
(ii) linearly graded bandgap and 2200 nm thickness, or
(iii) nonlinearly graded bandgap and 2000 nm thickness.

The optimal parameters for the bandgap in the CIGS layer are available in Tables 3–5. Both n_1 and n_2 were taken to be real-valued and independent of λ_0.

1. Optimal SLARC

First, we considered optimizing a SLARC by setting $L_{ARC2} = 0$. The parameter space for optimizing η was chosen as $L_{ARC1} \in [0, 1000]$ nm and $n_1 \in [1, 2.2]$. Scatter plots of the optimization results projected onto the $n_1-\eta$ and $L_{ARC1}-\eta$ planes are provided in Figs. S1–S3 of Supplement 1. Optimal combinations of the values of the parameters n_1 and L_{ARC1} are recorded in Table 6, along with the corresponding values of J_{sc}, V_{oc}, FF, and η.

The maximum efficiency predicted with the optimal homogeneous CIGS layer is 18.39%, and the optimal SLARC parameters are $n_1 = 1.40$ and $L_{ARC1} = 106$ nm. These parameters are very close to that of the 110-nm-thick MgF_2 ARC chosen for all previous calculations in this paper (as well as in Part I). The corresponding values of J_{sc}, V_{oc}, and FF are very close to that of the 110-nm-thick MgF_2 ARC. The maximum efficiency predicted with the optimal linearly graded-bandgap CIGS layer is 24.11%, and the optimal parameters are $n_1 = 1.40$ and $L_{ARC1} = 106$ nm. Again, these parameters are very close to that of the 110-nm-thick MgF_2 ARC, which however does reduce J_{sc} but enhances both FF and η ever so slightly compared to the optimal SLARC. The maximum efficiency predicted with the optimal nonlinearly graded-bandgap CIGS layer is 30.02%, and the optimal parameters are $n_1 = 1.40$ and $L_{ARC1} = 106$ nm. The 110-nm-thick MgF_2 ARC enhances J_{sc} and η but reduces both V_{oc} and FF slightly compared to the optimal SLARC.

Thus, the 110-nm-thick MgF_2 ARC performs almost as well as the optimal SLARC for the optimal CIGS solar cell, regardless of the type of bandgap grading.

2. Optimal DLARC

Finally, we considered optimizing DLARCs in the following parameter space: $L_{ARC1} \in [0, 1000]$ nm, $L_{ARC2} \in [0, 1000]$ nm, $n_1 \in [1, 2.2]$, and $n_2 \in [1, 2.2]$. Scatter plots of the optimization results projected onto the $n_1-\eta$, $n_2-\eta$, $L_{ARC1}-\eta$, and $L_{ARC2}-\eta$ planes are provided in Figs. S4–S6 of Supplement 1. Optimal combinations of the values of the parameters n_1, n_2, L_{ARC1}, and L_{ARC2} are provided in Table 6, along with the corresponding values of J_{sc}, V_{oc}, FF, and η.

Table 6. Predicted Optimal Parameters for SLARCs and DLARCs

Bandgap Grading	ARC Type	L_{ARC1} or L_{MgF_2} (nm)	L_{ARC2} (nm)	n_1 or n_{MgF_2}	n_2	J_{sc} (mA cm^{-2})	V_{oc} (mV)	FF (%)	η (%)	Relative Change in η (%)
Homogeneous	MgF_2	110	–	1.38 ± 0.01	–	31.86	700	82	18.39	
	SLARC	106	–	1.40	–	31.50	700	83	18.39	0
	DLARC	120	76	1.28	1.74	32.05	700	83	18.71	+1.74
Linear	MgF_2	110	–	1.38 ± 0.01	–	36.38	810	82	24.17	
	SLARC	106	–	1.40	–	36.59	810	81	24.11	−0.25
	DLARC	120	76	1.28	1.74	37.20	810	81	24.54	+1.78
Nonlinear	MgF_2	110	–	1.38 ± 0.01	–	38.02	980	80	29.98	
	SLARC	106	–	1.40	–	37.83	990	80	30.02	+0.13
	DLARC	120	76	1.28	1.74	38.47	990	80	30.57	+1.83

The maximum efficiency predicted with the optimal homogeneous CIGS layer is 18.71%, and the optimal DLARC parameters are $n_1 = 1.28$, $n_2 = 1.74$, $L_{ARC1} = 120$ nm, and $L_{ARC2} = 76$ nm. Compared to the 110-nm-thick MgF_2 ARC and the optimal SLARC, the relative increase in efficiency is just 1.74%. The same DLARC is optimal for the optimal solar cells with graded-bandgap CIGS photon-absorbing layers of either type, the relative increase in efficiency being about 1.8% compared to the 110-nm-thick MgF_2 ARC and the optimal SLARC.

We conclude that, whereas an optimal DLARC can increase the efficiency in comparison to an optimal SLARC, the increase will be very small and not worth the extra expense of depositing a second layer. Furthermore, the currently used 110-nm-thick MgF_2 layer performs almost as well as an optimal SLARC.

H. Computation Time

The optical-submodel code is the same for the solution algorithm of Part I as for the new solution algorithm, but the electrical-submodel codes in the two algorithms are different. The electrical-submodel code takes the bulk of computation time for one run of the optoelectronic model. In order to determine the change in computation time for one run with the previous algorithm (after removing the normalization error) and the new algorithm, we focused our attention on the optimal solar cell with the CIGS photon-absorbing layer of 600 nm thickness with (i) a homogeneous bandgap, (ii) a linearly graded bandgap, or (iii) a nonlinearly graded bandgap. The bandgap-grading parameters are provided in Tables 3–5. All computations for this comparison were performed on an NVIDIA Tesla K80 GPU with dual E5-2680 processors (24 total cores but access to 4 cores) and 256-GB RAM.

The three critical factors for the accuracy of the HDG scheme are the degree P_{deg} of the interpolating polynomials, the length of each element $d_z = z_{j+1} - z_j$, $\forall j \in [0, N-1]$, and the degree I_{deg} of quadrature integration. These were set equal to 5, 2 nm, and 10, respectively, as per error saturation criteria stated in Refs. [45,46]. For the FDM-based algorithm, we set $d_z = 1$ nm.

The computation times for one run are presented in Table 7. The new algorithm is about 10 times faster than the previous algorithm for the chosen solar cells. However, the HDG scheme uses high-order interpolating polynomials and has better accuracy than the FDM. The superiority of the new algorithm over the previous one in terms of computational cost definitely also varies with the bandgap-grading complexity and the number N of discretization steps. A detailed study in this regard is beyond the scope of this paper.

Table 7. Computation Times for One Run of the Optoelectronic Model, when the Electrical Submodel Is Implemented with the HDG-Based Algorithm of Part I [13] and the New FDM-Based Algorithm[a]

Bandgap Grading	Previous Algorithm (s)	New Algorithm (s)	Ratio
Homogeneous	1668	196	8.51
Linear	2813	276	10.19
Nonlinear	3398	287	11.83

[a]The solar cell's CIGS layer is 600 nm thick with bandgap-grading parameters provided in Tables 3–5.

Parenthetically, let us note that the HDG code approximates the particle densities directly, whereas the FDM approximates the quasi-Fermi potentials. An HDG method based on quasi-Fermi potentials would remove the issue of negative carrier densities and would be more directly comparable to the FDM.

4. CONCLUDING REMARKS

We presented a new algorithm based on the FDM to solve the 1D drift-diffusion system and thus improve the computational robustness and reduce the overall computational cost of optoelectronic optimization of thin-film CIGS solar cells with a graded-bandgap CIGS photon-absorbing layer and a flat backreflector. In doing so, we also removed a normalization error affecting the numerical results reported in Part I [13]. The CIGS layer has either (i) a homogeneous bandgap, or (ii) a linearly graded bandgap, or (iii) a nonlinearly graded bandgap. In addition, we revised the data on these solar cells illuminated by concentrated sunlight. Furthermore, we optimized the refractive indices and thicknesses of SLARCs and DLARCs for these solar cells.

Our new algorithm for the electrical submodel confirmed that optimal bandgap grading enhances the power-conversion efficiency by as much as 84% when the CIGS layer is 600 nm thick and 63% when the CIGS layer is 2200 nm thick. These efficiency enhancements are very similar to those reported in Part I, though specifics on the short-circuit current density and the open-circuit voltage were affected by the normalization

error. Bandgap grading provides the condition of large $E_g(z)$ in the proximity of the plane $z = L_d$ (which elevates V_{oc}), and there are regions in which $E_g(z)$ is small (which elevates the EHP generation rate); both of these characteristics are similar to those reported in Part I. Furthermore, a relative increase of efficiency by an additional 27% is possible if the sunlight were to be concentrated a hundredfold. A relative enhancement of no more than 2% is predicted with an optimal DLARC compared to the efficiency with an optimal SLARC, indicating that the simpler option of a SLARC may be economically preferable. The currently used 110-nm-thick layer of MgF_2 serves very well to reduce reflection losses, performing almost as well as an optimal SLARC. Finally, the new algorithm is significantly faster than the previous algorithm, and it is therefore preferable for rapid optoelectronic optimization.

Funding. National Science Foundation (DMS-2011996, DMS-2011603).

Acknowledgment. We thank an anonymous referee for a careful review of the original version of this paper. A. Lakhtakia thanks the Charles Godfrey Binder Endowment at the Pennsylvania State University for ongoing support of his research. The research of F. Ahmad and A. Lakhtakia was partially supported by the US NSF. The research of B. J. Civiletti and P. B. Monk was supported by the US NSF.

Disclosures. The authors declare no conflicts of interest.

Data availability. Data underlying the results presented in this paper are not publicly available at this time but may be obtained from the corresponding author upon reasonable request.

Supplemental document. See Supplement 1 for supporting content.

REFERENCES

1. BP p.l.c., *Statistical Review of World Energy 2021*, 70th ed. (BP, 2021).
2. P. Hawken, ed., *Drawdown: The Most Comprehensive Plan Ever Proposed to Reverse Global Warming* (Penguin, 2017).
3. McKinsey, *Global Energy Perspective 2022* (McKinsey, 2022).
4. C. S. Lai and M. D. McCulloch, "Levelized cost of electricity for solar photovoltaic and electrical energy storage," Appl. Energy **190**, 191–203 (2017).
5. M. Schmid, "Review on light management by nanostructures in chalcopyrite solar cells," Semicond. Sci. Technol. **32**, 043003 (2017).
6. C. van Lare, G. Yin, A. Polman, and M. Schmid, "Light coupling and trapping in ultrathin Cu(In,Ga)Se_2 solar cells using dielectric scattering patterns," ACS Nano **9**, 9603–9613 (2015).
7. J. Goffard, C. Colin, F. Mollica, A. Cattoni, C. Sauvan, P. Lalanne, J.-F. Guillemoles, N. Naghavi, and S. Collin, "Light trapping in ultrathin CIGS solar cells with nanostructured back mirrors," IEEE J. Photovolt. **7**, 1433–1441 (2017).
8. H. K. Raut, V. A. Ganesh, A. S. Nair, and S. Ramakrishna, "Anti-reflective coatings: a critical, in-depth review," Energy Environ. Sci. **4**, 3779–3804 (2011).
9. A. Polman, M. Knight, E. C. Garnett, B. Ehrler, and W. C. Sinke, "Photovoltaic materials: Present efficiencies and future challenges," Science **352**, aad4424 (2016).
10. M. Gloeckler and J. R. Sites, "Band-gap grading in Cu(In,Ga)Se_2 solar cells," J. Phys. Chem. Solids **66**, 1891–1894 (2005).
11. J. Song, S. S. Li, C. H. Huang, O. D. Crisalle, and T. J. Anderson, "Device modeling and simulation of the performance of Cu(In_{1-x},Ga_x)Se_2 solar cells," Solid-State Electron. **48**, 73–79 (2004).
12. B. Vermang, J. T. Wätjen, V. Fjällström, F. Rostvall, M. Edoff, R. Kotipalli, F. Henry, and D. Flandre, "Employing Si solar cell technology to increase efficiency of ultra-thin Cu(In,Ga)Se_2 solar cells," Prog. Photovolt: Res. Appl. **22**, 1023–1029 (2014).
13. F. Ahmad, T. H. Anderson, P. B. Monk, and A. Lakhtakia, "Efficiency enhancement of ultrathin CIGS solar cells by optimal bandgap grading," Appl. Opt. **58**, 6067–6078 (2019).
14. M. Faryad and A. Lakhtakia, "Enhancement of light absorption efficiency of amorphous-silicon thin-film tandem solar cell due to multiple surface-plasmon-polariton waves in the near-infrared spectral regime," Opt. Eng. **52**, 087106 (2013).
15. M. Faryad and A. Lakhtakia, "Enhancement of light absorption efficiency of amorphous-silicon thin-film tandem solar cell due to multiple surface-plasmon-polariton waves in the near-infrared spectral regime: errata," Opt. Eng. **53**, 129801 (2014).
16. L. Liu, M. Faryad, A. S. Hall, G. D. Barber, S. Erten, T. E. Mallouk, A. Lakhtakia, and T. S. Mayer, "Experimental excitation of multiple surface-plasmon-polariton waves and waveguide modes in a one-dimensional photonic crystal atop a two-dimensional metal grating," J. Nanophotonics **9**, 093593 (2015).
17. F.-J. Haug, K. Söderström, A. Naqavi, and C. Ballif, "Excitation of guided-mode resonances in thin film silicon solar cells," MRS Symp. Proc. **1321**, 123–128 (2011).
18. T. Khaleque and R. Magnusson, "Light management through guided-mode resonances in thin-film silicon solar cells," J. Nanophoton. **8**, 083995 (2014).
19. T. H. Anderson, M. Faryad, T. G. Mackay, A. Lakhtakia, and R. Singh, "Combined optical-electrical finite-element simulations of thin-film solar cells with homogeneous and nonhomogeneous intrinsic layers," J. Photon. Energy **6**, 025502 (2016).
20. T. H. Anderson, T. G. Mackay, and A. Lakhtakia, "Enhanced efficiency of Schottky-barrier solar cell with periodically nonhomogeneous indium gallium nitride layer," J. Photon. Energy **7**, 014502 (2017).
21. J. A. Polo, Jr., T. G. Mackay, and A. Lakhtakia, *Electromagnetic Surface Waves: A Modern Perspective* (Elsevier, 2013).
22. I. Sharma, P. S. Pawar, R. K. Yadav, R. Nandi, and J. Heo, "Review on bandgap engineering in metal-chalcogenide absorber layer via grading: a trend in thin-film solar cells," Solar Energy **246**, 152–180 (2022).
23. M. G. Moharam, D. A. Pommet, E. B. Grann, and T. K. Gaylord, "Stable implementation of the rigorous coupled-wave analysis for surface-relief gratings: enhanced transmittance matrix approach," J. Opt. Soc. Am. A **12**, 1077–1086 (1995).
24. F. Ahmad, A. Lakhtakia, and P. B. Monk, *Theory of Graded-Bandgap Thin-Film Solar Cells* (Morgan & Claypool, 2021).
25. T. G. Mackay and A. Lakhtakia, *The Transfer-Matrix Method in Electromagnetics and Optics* (Morgan & Claypool, 2020).
26. D. Brinkman, K. Fellner, P. A. Markowich, and M.-T. Wolfram, "A drift-diffusion-reaction model for excitonic photovoltaic bilayers: asymptotic analysis and a 2-D HDG finite-element scheme," Math. Models Methods Appl. Sci. **23**, 839–872 (2013).
27. R. J. LeVeque, *Finite Difference Methods for Ordinary and Partial Differential Equations: Steady State and Time Dependent Problems* (SIAM, 2007).
28. F. Ahmad, A. Lakhtakia, and P. B. Monk, "Enhanced efficiency of graded-bandgap thin-film solar cells due to concentrated sunlight," Appl. Opt. **60**, 10570–10578 (2021).
29. P. W. Baumeister, *Optical Coating Technology* (SPIE, 2004).
30. F. Chen and L. Wang, *Light Trapping Design in Silicon-Based Solar Cells* (INTECH, 2011).
31. S. A. Boden and D. M. Bagnall, "Optimization of moth-eye antireflection schemes for silicon solar cells," Prog. Photovolt. Res. Appl. **18**, 195–203 (2010).
32. N. Yamada, T. Ijiro, E. Okamoto, K. Hayashi, and H. Masuda, "Optimization of anti-reflection moth-eye structures for use in crystalline silicon solar cells," Opt. Express **19**, A118–A125 (2011).
33. S.-Y. Lien, D.-S. Wuu, W.-C. Yeh, and J.-C. Liu, "Tri-layer antireflection coatings (SiO_2/SiO_2-TiO_2/TiO_2) for silicon solar cells using a sol–gel technique," Sol. Energy Mater. Sol. Cells **90**, 2710–2719 (2006).
34. U. Sikder and M. A. Zaman, "Optimization of multilayer antireflection coating for photovoltaic applications," Opt. Laser Technol. **79**, 88–94 (2016).
35. M. J. Dodge, "Refractive properties of magnesium fluoride," Appl. Opt. **23**, 1980–1985 (1984).
36. N. Ehrmann and R. Reineke-Koch, "Ellipsometric studies on ZnO:Al thin films: refinement of dispersion theories," Thin Solid Films **519**, 1475–1485 (2010).
37. C. Stelling, C. R. Singh, M. Karg, T. A. F. König, M. Thelakkat, and M. Retsch, "Plasmonic nanomeshes: their ambivalent role as

transparent electrodes in organic solar cells," Sci. Rep. **7**, 42530 (2017).
38. R. E. Treharne, A. Seymour-Pierce, K. Durose, K. Hutchings, S. Roncallo, and D. Lane, "Optical design and fabrication of fully sputtered CdTe/CdS solar cells," J. Phys. Conf. Ser. **286**, 012038 (2011).
39. S. Minoura, T. Maekawa, K. Kodera, A. Nakane, S. Niki, and H. Fujiwara, "Optical constants of Cu(In,Ga)Se_2 for arbitrary Cu and Ga compositions," J. Appl. Phys. **117**, 195703 (2015).
40. F. Ahmad, T. H. Anderson, P. B. Monk, and A. Lakhtakia, "Optimization of light trapping in ultrathin nonhomogeneous $CuIn_{1-\xi}Ga_{\xi}Se_2$ solar cell backed by 1D periodically corrugated backreflector," Proc. SPIE **10731**, 107310L (2018).
41. R. Boidin, T. Halenkovič, V. Nazabal, L. Beneš, and P. Němec, "Pulsed laser deposited alumina thin films," Ceram. Int. **42**, 1177–1182 (2016).
42. M. R. Querry, "Optical constants of minerals and other materials from the millimeter to the ultraviolet," Contractor Report CRDEC-CR-88009 (1987).
43. National Renewable Energy Laboratory, "Reference solar spectral irradiance: air mass 1.5," 2022, https://www.nrel.gov/grid/solar-resource/spectra-am1.5.html.
44. F. Brezzi, L. Marini, S. Micheletti, P. Pietra, R. Sacco, and S. Wang, "Discretization of semiconductor device problems (I)," in *Handbook of Numerical Analysis: Numerical Methods for Electrodynamic Problems*, W. Schilders and E. ter Maten, eds. (North-Holland, 2005), pp. 317–342.
45. T. H. Anderson, B. J. Civiletti, P. B. Monk, and A. Lakhtakia, "Coupled optoelectronic simulation and optimization of thin-film photovoltaic solar cells," J. Comput. Phys. **407**, 109242 (2020).
46. T. H. Anderson, B. J. Civiletti, P. B. Monk, and A. Lakhtakia, "Coupled optoelectronic simulation and optimization of thin-film photovoltaic solar cells: errata," J. Comput. Phys. **418**, 109561 (2020).
47. Y. Jaluria, *Computer Methods for Engineering* (Taylor & Francis, 1996).
48. J. Nocedal and S. J. Wright, *Numerical Optimization*, 2nd ed. (Springer, 2006).
49. R. Storn and K. Price, "Differential evolution—a simple and efficient heuristic for global optimization over continuous spaces," J. Global Optim. **11**, 341–359 (1997).
50. J. Abushama, R. Noufi, S. Johnston, S. Ward, and X. Wu, "Improved performance in $CuInSe_2$ and surface-modified $CuGaSe_2$ solar cells," in *Proceedings 31st IEEE Photovoltaic Speciality Conference (PVSC)*, Lake Buena Vista, Florida, June 3–7, 2005, pp. 299–302.
51. P. Jackson, R. Wuerz, D. Hariskos, E. Lotter, W. Witte, and M. Powalla, "Effects of heavy alkali elements in Cu(In,Ga)Se_2 solar cells with efficiencies up to 22.6%," Phys. Status Solidi RRL **10**, 583–586 (2016).
52. S. J. Fonash, *Solar Cell Device Physics* (Academic, 2010).
53. B. L. Smith, M. Woodhouse, K. A. W. Horowitz, T. J. Silverman, J. Zuboy, and R. M. Margolis, "Photovoltaic (PV) module technologies: 2020 benchmark costs and technology evolution framework results," NREL/TP-7A40-78173 (National Renewable Energy Laboratory, 2021), https://www.nrel.gov/docs/fy22osti/78173.pdf.
54. M. A. Green, "Photovoltaic technology and visions for the future," Prog. Energy **1**, 013001 (2019).
55. H. Cotal, C. Fetzer, J. Boisvert, G. Kinsey, R. King, P. Hebert, H. Yoon, and N. Karam, "III–V multijunction solar cells for concentrating photovoltaics," Energy Environ. Sci. **2**, 174–192 (2009).
56. J. Nelson, *The Physics of Solar Cells* (Imperial College, 2003).